

# Experimental and Numerical Investigation of CH<sub>4</sub>/O<sub>2</sub> Rocket Combustors



Nikolaos Perakis and Oskar J. Haidn

**Abstract** The experimental investigation of sub-scale rocket engines gives significant information about the combustion dynamics and wall heat transfer phenomena occurring in full-scale hardware. At the same time, the performed experiments serve as validation test cases for numerical CFD models and for that reason it is vital to obtain accurate experimental data. In the present work, an inverse method is developed able to accurately predict the axial and circumferential heat flux distribution in CH<sub>4</sub>/O<sub>2</sub> rocket combustors. The obtained profiles are used to deduce information about the injector-injector and injector-flame interactions. Using a 3D CFD simulation of the combustion and heat transfer within a multi-element thrust chamber, the physical phenomena behind the measured heat flux profiles can be inferred. A very good qualitative and quantitative agreement between the experimental measurements and the numerical simulations is achieved.

## 1 Introduction

A very important step in the process of designing and optimizing new components or subsystems for rocket propulsion devices is the numerical simulation of the flow and combustion in them. Implementing CFD tools in the design process significantly reduces the development time and cost and allows for greater flexibility. The main requirements that a successful CFD tool must fulfill in order to be suitable for rocket

---

N. Perakis (✉) · O. J. Haidn  
Chair of Space Propulsion, Technical University of Munich, Boltzmannstr. 15, 85748 Garching, Germany  
e-mail: [nikolaos.perakis@tum.de](mailto:nikolaos.perakis@tum.de)

O. J. Haidn  
e-mail: [haidn@tum.de](mailto:haidn@tum.de)

© The Author(s) 2021  
N. A. Adams et al. (eds.), *Future Space-Transport-System Components under High Thermal and Mechanical Loads*, Notes on Numerical Fluid Mechanics and Multidisciplinary Design 146, [https://doi.org/10.1007/978-3-030-53847-7\\_23](https://doi.org/10.1007/978-3-030-53847-7_23)

engine applications is providing an accurate description of the heat loads on the chamber wall, the combustion pressure, combustion efficiency as well as performance parameters such as the specific impulse [8].

A significant step during the development of numerical tools for combustion and turbulence modeling in rocket engines is the validation of the models. For this process, the design and testing of sub-scale engines is required. Specifically, before the design of full-scale engines, tests using single-element and multi-element sub-scale hardware are performed [2, 10, 12, 15]. The knowledge about the performance of the injector elements, i.e. the mixing of the propellants, the injector/injector interaction and injector/wall interaction in the sub-scale experiments is used as an input for the improvement of the full-scale design without the need for costly full-scale testing. The test data obtained from the sub-scale configurations are then used to provide validation data for numerical simulations. The need for this data over a wide range of operational conditions is even more critical for the innovative propellant combination of methane/oxygen due to the limited number of available tests [5, 9, 18, 22, 26].

Of the experimentally available quantities, the one having the largest significance for the understanding of the physical and chemical phenomena is the heat flux. Given the limited access to the burning gas, the heat flux distributions are usually utilized to deduce information about the conditions within the chamber. Moreover the prediction of the engine's lifetime, the design of an effective cooling system and the reliability of the chamber components after a specific number of tests is imminently connected to the heat loads applied onto the chamber wall thereby increasing the importance of this quantity even more.

Within the framework of facilitating the development of CFD for rocket engines, several different configurations of rocket combustors and propellant combinations have been tested as part of the Transregio 40 as shown in Silvestri et al. [23], building an experimental database which can be used in the validation process of CFD models. In this project, the accurate experimental determination of the heat loads and the numerical prediction of the wall heat transfer have a vital role.

For that reason, the present work introduces an inverse method for the evaluation of the heat transfer in actively cooled rocket engines, which can be applied to the evaluation of axially and circumferentially varying heat loads in multi-element sub-scale and full-scale rocket thrust chambers with minimal computational cost. The method is applied for the evaluation of the heat loads in a GOX/GCH<sub>4</sub> multi-element chamber giving information about the flow-field, heat release and injector/injector interaction. Numerical results obtained by 3D CFD simulations of the combustion and heat transfer within the combustion chamber are then compared to the obtained measurements.

## 2 Description of the Test Case

The examined multi-injector combustion chamber was designed for GOX and GCH<sub>4</sub> allowing high chamber pressures (up to 100 bar) and film cooling behavior examination. One of the key aspects of the project is to improve the knowledge on heat transfer processes and cooling methods in the combustion chamber, which is mandatory for the engine design. The attention is focused, in particular, on injector-injector and injector-wall interaction. In order to have a first characterization of the injectors' behavior, the multi-element combustion chamber is tested at low combustion chamber pressures and for a wide range of mixture ratios [23].

The seven-element rocket combustion chamber has an inner diameter of 30 mm and a contraction ratio of 2.5 in order to achieve Mach numbers similar to the ones in most rocket engine applications. The combustion chamber, depicted in Fig. 1, consists of four cylindrical water cooled chamber segments, as well as a nozzle segment (individually cooled), adding up to a total length of 382 mm. Seven shear coaxial injector elements are integrated and the test configuration includes the GOX post being mounted flush with respect to the injection face. Figure 3 shows the injector configuration, as well as the locations of the cooling channels in segment A.

For the present test case an operating point with mean combustion chamber pressure of 18.3 bar and mixture ratio of 2.65 is chosen. For the cooling system, two separate cooling cycles are implemented: one for the first four segments in the combustion chamber and an additional cooling cycle for the nozzle segment. The cross sections of the cooling channels in segments A-D are shown in Fig. 3.

Wall temperature values are available at radial distances of 0.7–1.5 mm from the hot gas wall. Each of the 8 axial positions equipped with thermocouples, alternates between 0.7 and 1.5 mm, with the first location at 2.5 mm downstream of the injector having a hot gas wall distance of 1.5 mm. Type T thermocouples with 0.5 mm diameter are installed to measure the temperature within the structure. The locations of

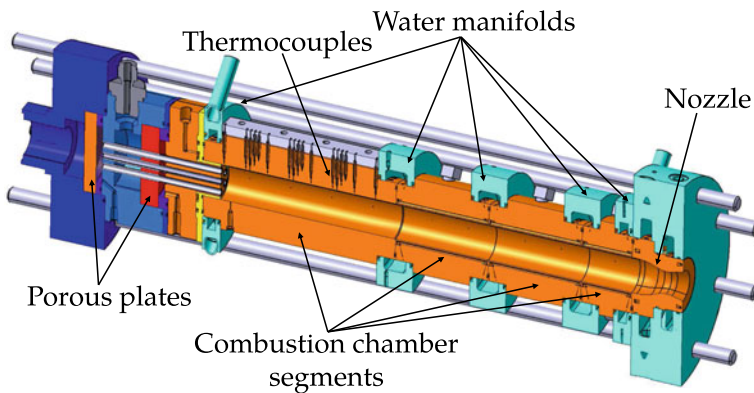


Fig. 1 Sketch of the combustion chamber

the thermocouples relative to the cooling channels are shown in the right sub-figure of Fig. 4. The inner part of the chamber (until the radius corresponding to the end of the cooling channels) consists of a CuCrZr alloy, whereas the outer part has been manufactured using copper electroplating.

### 3 Inverse Heat Transfer Method

Experimental lab-scale rocket combustors cooled by a water cycle or other cooling medium have the characteristic property of reaching a steady state temperature distribution after the first seconds of operation. This effect is utilized when evaluating the heat flux profiles, since the latter ones can simply be obtained from the enthalpy difference of the outgoing and incoming coolant flow. This calorimetric method however only provides average values and its resolution is given by the number of cooling segments. For a more detailed distribution, the temperature field has to be reconstructed using an inverse method.

Inverse heat transfer methods have been successfully applied for the heat flux estimation in capacitively cooled engines where the temperature field is not stationary during the test operation and hence a transient inverse heat conduction method is needed [4, 19, 27]. The main concept behind an inverse method for heat conduction problems lies in trying to estimate the boundary conditions (causes) which best fit the measured temperature values (effects) while keeping the physics of the problem intact. Apart from the hot gas wall, a second boundary condition is present in the system, namely the heat transfer between the coolant and the structure. The modeling of the heat transfer can be performed using one-dimensional Nusselt correlations. Despite their empirical nature and lower sophistication level compared to CFD, their fast implementation and minimal computational resources render them attractive for test data evaluation. In the present work, this particular method is employed due to the limited number of thermocouples installed on the examined hardware and the need for short evaluation times.

Similarly to the majority of inverse algorithms, the method is based on an iterative approach as outlined in Fig. 2. The goal of the optimization is to minimize the difference between the measured and calculated temperatures at the measurement locations. The inverse method is implemented in the Ro $\dot{q}$ FITT code which has already been validated for the evaluation of rocket engines in Perakis et al. [19].

The starting point of the code is to initialize the temperature in the computational domain and to choose an initial guess for the heat flux. With the initial conditions (temperature field) and the boundary conditions (guessed heat flux) the material properties of the coolant are calculated and the heat transfer coefficient are obtained via the Nusselt correlation. After that, the first step is solving the direct heat transfer problem.

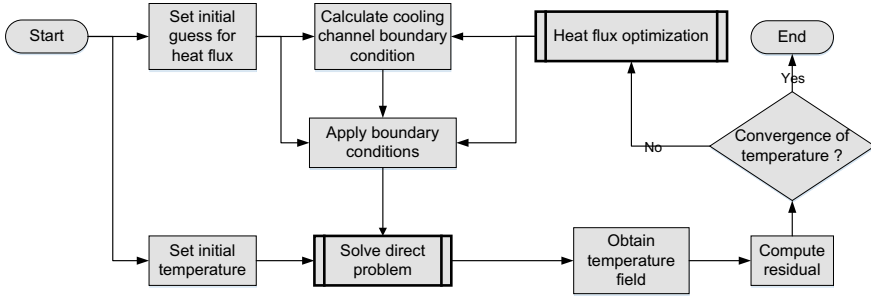


Fig. 2 Inverse heat transfer iterative algorithm

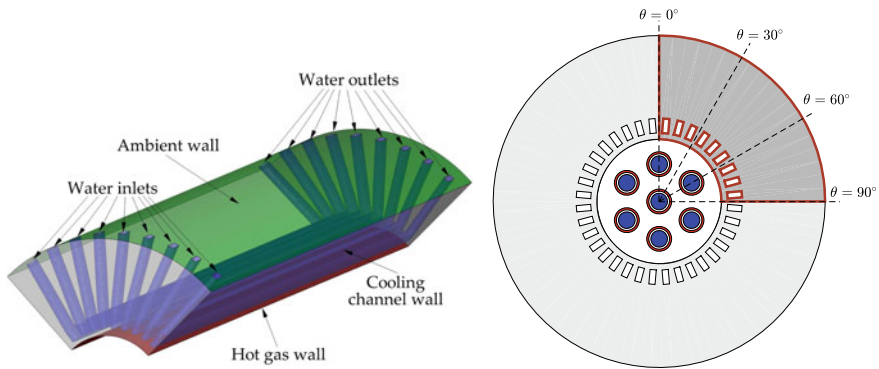


Fig. 3 Schematic view of the first chamber segment (left) and cut through the combustion chamber (right)

### 3.1 Direct Solver

For the solution of the thermal conduction problem, the commercial tool ANSYS Fluent [7] is used and a file-based interface to the code RoqFITT is programmed. The heat conduction equation (Eq. 1) is solved using a finite volume method in an unstructured grid consisting of 7.5 million cells.

$$\nabla^2 T = 0 \tag{1}$$

The direct solver is used to solve the heat conduction partial differential equation (PDE) in a simplified geometry. The geometry consists only of the combustion chamber and does not include the fluid domain. The effect of the coolant on the temperature field of the structure is included by specifying the modeled boundary conditions. Only the first segment of the combustion chamber is included in the computational domain, since the number of the installed thermocouples in the other segments is too low for a sufficient resolution of the heat flux profiles using the inverse method. The interfaces between the first and second segment as well as

between the injector head and the first segment are defined as adiabatic. Finally, a natural convection boundary condition is applied to the outer wall with a convective heat transfer coefficient  $h = 10W/(m^2 \cdot K)$  and an ambient temperature corresponding to the one measured at each test. An overview of the computational domain and the corresponding boundaries is given in Fig. 3.

The orientation of the chosen segment with regards to the injector elements is given in Fig. 3. The light gray area shows the entire chamber domain, whereas the area highlighted in dark grey is the modeled domain. The red lines represent the boundaries of the domain. The  $\theta = 0^\circ$  and  $\theta = 60^\circ$  positions correspond to azimuthal locations directly above an injector element, whereas  $\theta = 30^\circ$  and  $\theta = 90^\circ$  are symmetry planes between two adjacent elements.

The optimized (hot gas wall) and the modeled (cooling channel) boundary conditions are applied respectively as

$$\dot{q} = \lambda \frac{\partial T}{\partial \mathbf{n}} \Big|_S \quad (2)$$

$$h_{cc}(T_{cc} - T_w) = \lambda \frac{\partial T}{\partial \mathbf{n}} \Big|_S \quad (3)$$

In this context  $\mathbf{n}$  is the outward pointing normal vector. Upon solving the direct problem, the temperature field is known and hence the calculated value of the temperature at all the thermocouple positions can be extracted and compared with the measured ones. This residual temperature difference is given as an input to the optimization algorithm.

### 3.2 Optimization Method

The purpose of the optimization is to minimize the difference between the calculated ( $\mathbf{T}_c$ ) and measured ( $\mathbf{T}_m$ ) temperatures. This residual  $J$  which is subject to minimization is defined as in Eq. 4:

$$J(\mathbf{P}) = [\mathbf{T}_m - \mathbf{T}_c(\mathbf{P})]^T [\mathbf{T}_m - \mathbf{T}_c(\mathbf{P})] \quad (4)$$

The vector  $\mathbf{P}$  describes the heat flux values at the parameter points which are subject to optimization. The heat flux is a continuous variable being applied to all the points, however optimizing the heat flux value at every single point in contact with the hot gas would be computationally expensive and render the problem more ill-posed [1]. For the method presented here, a parameter is placed only at locations which possess at least one temperature sensor, so the number of parameters  $N$  is always smaller or equal to the thermocouple number  $M$ . At each time step, the values of the  $N$  parameter points are changed to reduce the residual  $J$ .

RoqFITT utilizes an iterative update by means of the Jacobi matrix  $\mathbf{S}$ , which serves as a sensitivity matrix describing the change of the temperature at a thermocouple position due to a small change at a specific heat flux parameter value. Its structure is presented in Eq. 5. It was shown in a sensitivity study that the linearity of the Fourier heat conduction equation allows for a calculation of the Jacobi matrix outside of the optimization loop. For that reason the computation of the matrix occurs as a pre-processing step before the calculation and it is saved for future calculations as well.

$$\mathbf{S} = [S_{ij}] = \left[ \frac{\partial T_i}{\partial P_j} \right] \quad (5)$$

The implemented optimization method is based on a linearization of the problem and follows the Newton–Raphson formulation for the solution of non-linear systems [6]. The heat flux at each iteration step  $k$  is obtained by solving the algebraic equation

$$\mathbf{S} \cdot \mathbf{P}^{k+1} = [\mathbf{T}_m - \mathbf{T}_c(\mathbf{P}^k)] + \mathbf{S} \cdot \mathbf{P}^k \quad (6)$$

The process is repeated until convergence is achieved, i.e. until the residual drops beneath a predefined value  $\varepsilon$ .

### 3.3 Applying the Heat Flux on the Boundary

At each axial position with available temperature measurements, four thermocouples are installed, each one at 0°, 30°, 60° or 90°. In total 8 axial positions are equipped with thermocouples leading to 32 sensors used in each calculation. The possible locations of the thermocouples are shown in the right sub-figure of Fig. 4, where the orange markers represent the 1.5 mm and the red ones the 0.5 mm distance from the hot gas wall. A cubic interpolation is used to transform the discrete values to a continuous profile in axial and azimuthal direction. At the symmetry planes (0° and 90°) a symmetry condition is applied for the interpolation of the heat flux in azimuthal direction, meaning  $\partial \dot{q} / \partial \theta = 0$ . For the axial positions between the last thermocouple and the end of the chamber segment, a linear extrapolation is applied.

### 3.4 Modeling the Cooling Channels

For the unknown heat transfer coefficient in the cooling channels, Nusselt correlations for generic pipe flows are implemented. Using the work of Kirchberger et al. [13, 14] where correlations were used for the description of the cooling channel heat transfer, the Kraussold model is utilized. The Kraussold correlation which reads

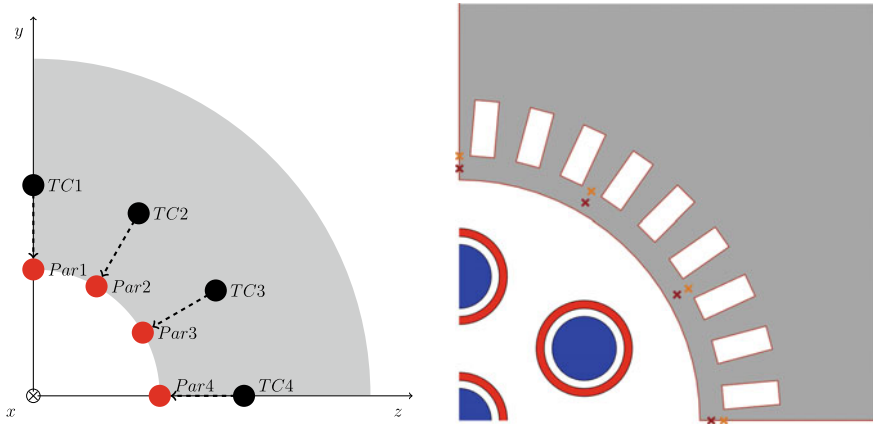


**Fig. 4** Definition of parameter points (left) and the locations of installed thermocouples (right)

$$Nu_{cc} = \frac{h_{cc} \cdot d_h}{\lambda} = 0.024 \cdot Re^{0.8} \cdot Pr^{0.37} \quad (7)$$

is a function of the geometry (hydraulic diameter  $d_h$ ) and material properties as it depends on the heat capacity  $c_p$ , thermal conductivity  $\lambda$ , dynamic viscosity  $\mu$  as well as on the mass flow rate  $\dot{m}_{cc}$  (which is needed for the Reynolds number). The temperature dependent properties are obtained using the NIST database [17]. More details about the method can be found in [21].

## 4 Experimental Results

Using the inverse method, azimuthal heat flux distributions which are not available via the calorimetric method are obtained.

### 4.1 Experimental Azimuthal Heat Flux Profiles

The azimuthal heat flux profiles are illustrated in Fig. 5. For each axial position, the heat flux resulting from the inverse method is plotted with the markers representing the values at the parameter points and the solid lines representing the azimuthal heat flux profile applied at the wall. The uncertainty intervals calculated as described in [21] are shown as shadows and amount to  $\pm 10\%$ – $30\%$  of the average values.

It is easy to notice by looking at Fig. 5 that an injector footprint is visible in the heat flux data. Specifically, for the first 60 mm of the chamber a local maximum directly above the injector is observed with a local minimum at the positions between



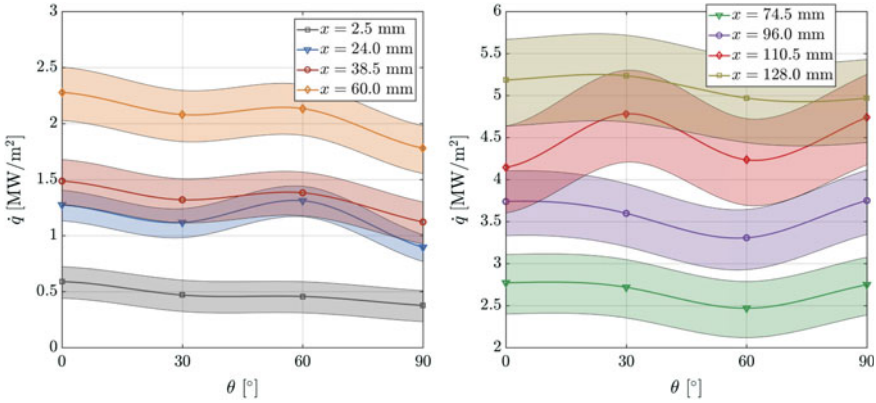


**Fig. 5** Heat flux profiles along the azimuthal direction for different axial positions. The corresponding uncertainty intervals are also shown

two elements (30° and 90°). Despite the asymmetry produced by the temperature readings, all four available axial positions show a similar trend.

Moving towards positions downstream, a shift is observed in the measured heat flux profiles. Starting at around 74.5 mm the heat flux at the 60° position appears to drop below the values at 30° and 90°, indicating a change in the injector/injector and injector/wall interaction. Due to the asymmetry in the measured temperatures, the 0° heat flux undergoes this shift at a later downstream position and the profile becomes symmetric again at the 110.5 mm position. After this axial location, the injector footprint is inverted compared to the initial positions close to the face-plate.

For axial positions close to the face-plate, the flames from the individual injector elements are almost cylindrical and interact minimally with each other. Therefore, the heat transfer coefficient directly above the injector is maximal due to the distance between element and wall being smallest. As the heat release in the coaxial shear layer of each element increases and leads to a radial expansion of the jet outwards, the interaction between the jets is amplified. In an effort to expand radially against each other, the flames build a stagnation flow between two neighboring elements. Due to the central element jet also expanding radially outwards, the stagnation flow is forced towards the wall and increases the local heat transfer at the locations between the injectors. Further downstream (for positions which are unfortunately in the other 3 segments of the TUM chamber and hence not shown in the inverse method results) the mixing is further increased and a homogeneous flow is achieved, leading to a smoother heat flux distribution where the injector footprint is no longer visible. This pattern is also observed in CFD simulations in Sect. 5.

The effect of the injector footprint that the inverse method tries to capture requires a resolution of at least 30°, namely equal to half the angular distance between the injectors. The chosen hardware is equipped with sensors satisfying this minimal angular resolution, meaning that any heat flux information with a shorter angular

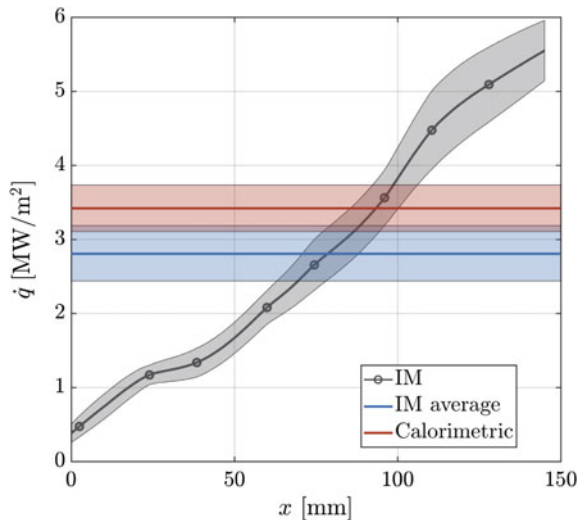
wavelength will not be captured by the method. An increase in the number of installed sensors or a rotation of the hardware after every test repetition as in the work of Suslov et al. [25] would be required for a more detailed profile.

## 4.2 Comparison with Calorimetric Method

Looking at the azimuthally averaged profile and globally average heat flux value in Fig. 6, a comparison with the calorimetrically determined value can be made. Using the difference of incoming and outgoing water enthalpy flow, the calorimetric heat flux lies at  $3.40 \text{ MW/m}^2$  with a relative error of approximately 10%. The error comes from the uncertainty of the water mass flow measurement (around 1% of the nominal value) and a 1 K accuracy of each water thermocouple. The average value obtained via the inverse method on the other hand is equal to  $2.85 \text{ MW/m}^2$  with a 11.5% uncertainty. The uncertainty intervals of the two heat flux evaluation methods intersect, which serves as a validation for the heat flux level predicted by the inverse method.

The deviation between the two methods is attributed to the error introduced by the generic Nusselt correlation for the specific geometry, which could underestimate the heat transfer coefficient within the cooling channels. Due to the shape of the channels, a recirculation zone is namely expected at the interface between the radial part and the flow-parallel part of the channel, which could theoretical increase the local turbulence and heat pickup. The heat flux obtained by the inverse method is directly proportional to the heat flux exiting the domain through the cooling channels. Hence too small a value for  $h_{cc}$  would directly cause a lower wall heat flux compared

**Fig. 6** Average heat flux along axial position (right)



to the experiment. Further studies are planned in order to evaluate the validity of the chosen correlation using comparison with CFD simulations of the cooling channels and to derive a new correlation fitted for the present flow configuration.

## 5 Numerical Simulation

In order to better understand the flame-flame and flame-wall interaction which gives rise to the measured heat flux profiles, a CFD simulation is carried out. The numerical simulation of the turbulent combustion within the seven-element chamber is carried out using the pressure-based code ANSYS Fluent, in which the 3D RANS equations are solved.

### 5.1 Computational Setup

The computational domain considered in the RANS calculation of the turbulent combustion consists of a 30° segment of the thrust chamber, which includes only half injector in the outer row and correspond to 1/12th of the whole chamber. In order to create a developed velocity profile at the injection plane, the injector tubes are also modeled as can be seen in Fig. 7. The final mesh consists of 2.9 million cells and is chosen after a mesh convergence study. In order to resolve the boundary layer appropriately and to facilitate a correct heat load prediction, the mesh in the vicinity of walls is refined as to satisfy the condition  $y^+ \approx 1$ . A close-up view of the mesh at the injector and faceplate is shown in Fig. 8. The black cells represent the post-tip between oxygen and fuel and the red and blue cells the CH<sub>4</sub> and O<sub>2</sub> inlets respectively. The grid is chosen after a grid convergence study, which is shown in [20].

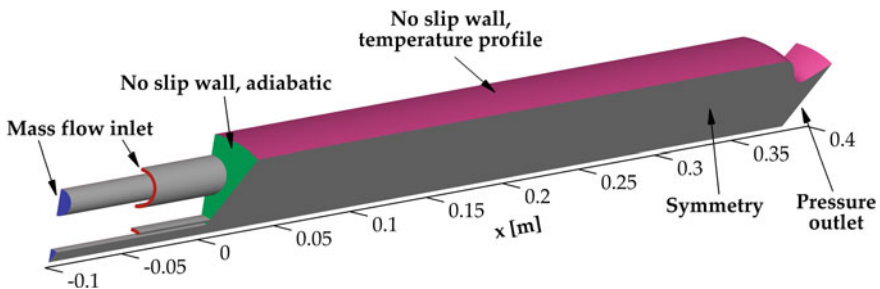
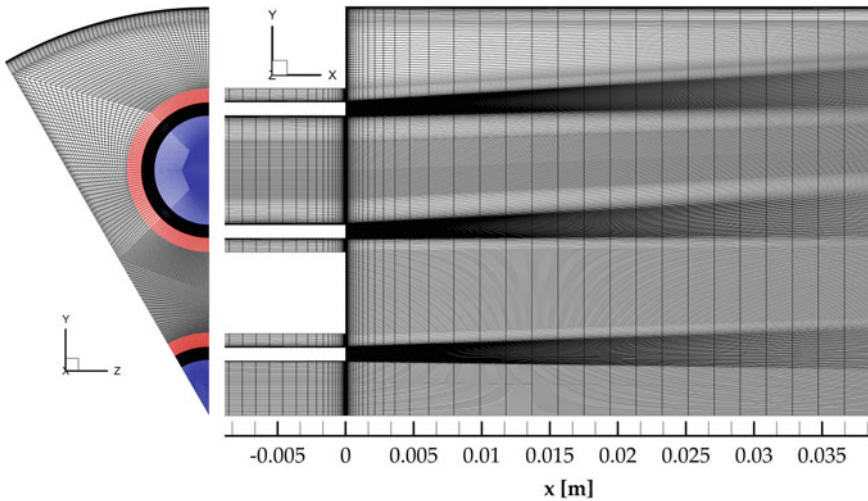


Fig. 7 Computational domain and applied boundary conditions



**Fig. 8** Mesh at injector elements, faceplate and symmetry plane

### 5.1.1 Boundary Conditions

A schematic representation of the applied boundary conditions can be seen in Fig. 7. The oxygen and methane inlets of the coaxial injector are defined as mass flow inlets by prescribing the appropriate values from the experiments. For the outlet a pressure boundary condition is applied. The planes corresponding to 0 and 30° are defined as symmetry boundary conditions. This is chosen to reduce the computational time of the simulation and to take advantage of the RANS formulation which gives only the mean flow values. At the chamber wall, a prescribed temperature profile is defined. This profile is obtained by the experimental values. All remaining walls are defined as adiabatic thermal boundaries and are given a no-slip condition.

### 5.1.2 Numerical Models

The flowfield in the combustion chamber is described by the conservation equations for mass, momentum and energy in three dimensional space. For the closure of the viscous stress tensor, the standard  $k-\epsilon$  model proposed by Launder and Spalding [16] is employed. To account for the proper treatment of the wall, the two-layer approach by Wolfshtein [29] is implemented.

NASA polynomials are implemented for the enthalpy and heat capacity of the individual species, while the mixture values are obtained using a mass fraction averaging. A pressure based scheme is used for the solution of the discretized equations. Density and pressure are coupled through the ideal gas equation of state.

The chemistry modeling takes place by using the steady flamelet approach, which significantly reduces the computational resources required for combustion simulations by reducing the number of transport equations. The reaction mechanism used for the solution of the flamelets is the one by Slavinskaya et al. [24] and consists of 21 species and 97 reactions. For the molecular transport (viscosity and thermal conductivity) the Chapman-Enskog kinetic theory [3, 11] is utilized for the individual species, combined with the Wilke mixture rule [28].

## 5.2 Temperature and Heat Release

In Fig. 9 the temperature field inside the thrust chamber is plotted. Although a 30° domain is simulated, a larger domain (150°) is shown in the plots for a more intuitive visual representation. In the same plot, the line corresponding to stoichiometric composition ( $Z_{st} = 0.2$ ) in the case of CH<sub>4</sub>/O<sub>2</sub> combustion is indicated. This is included to give an insight into the shape of the flame and consequently its length.

By examining the distribution, it is evident that the mixing of the oxidizer and fuel progresses with increasing axial distance from the face-plate. Specifically, the initial temperature stratification remains restricted to the first two thirds of the engine and a more homogeneous field is present further downstream. The initial stratification indicates that for positions close to the face-plate, the gas is not entirely mixed and that the heat release due to combustion is still ongoing.

The fields of heat release rate in Fig. 9 confirm this assumption and give a more detailed view into the mixing within the chamber. As expected the main heat release takes place within the shear layer, where the scalar dissipation rate is highest. The energy release continues along the stoichiometric lines further downstream and drops below 1% of the maximal value before the end of the chamber.

## 5.3 Axial Heat Flux Results

A comparison with the average axial heat flux profile of the experimental methods (calorimetric and inverse) is given in Fig. 10. Starting from the positions close to the injector, the heat flux from the CFD appears to rise before dropping shortly at around 10 mm from the face-plate. This indicates the location of a recirculation zone, which creates a stagnation point and hence an increase in the local heat transfer. The inverse profile shows a similar trend, but not so prominent, as a slight plateau is achieved at 25 mm. Due to the axial resolution of the heat flux, it is difficult to resolve the small recirculation zone which is predicted by the CFD, but the small drop in the heat flux increase indicates that this effect is still captured by the temperature measurements.

Downstream of this position both methods predict a steady increase of the heat flux value and after 110 mm they both show a slower increment, as the profile starts flattening out. This is caused by the build-up of the thermal boundary layer at the

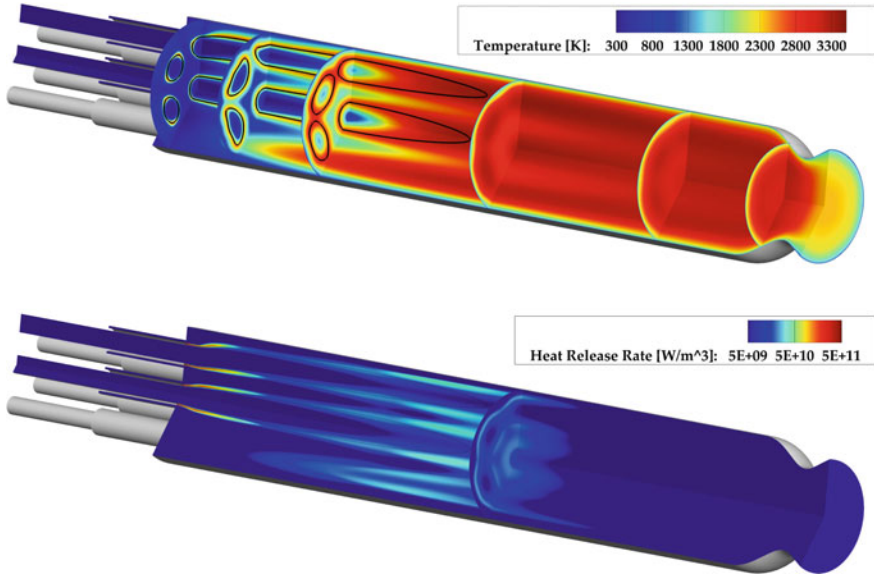


**Fig. 9** Temperature (top) and heat release (bottom) field in the thrust chamber. The black line corresponds to the stoichiometric mixture fraction. Axial scaling 50%

wall and the fact that the heat release in the chamber is reduced for positions further downstream.

When examining the average values, the CFD simulation delivers  $2.93 \text{ MW/m}^2$ , which is comparable to the inverse method result and lies around 14.5% lower than the calorimetric value for this segment.

#### 5.4 Azimuthal Heat Flux Results

The azimuthal profile of the heat flux at the wall is shown in Fig. 11. Here  $0^\circ$  corresponds to the position directly above the injector and  $-30^\circ$ ,  $30^\circ$  to the symmetry planes, while 0 mm refers to the faceplate and 300 mm is a plane approximately 40 mm before the end of the combustion chamber and the beginning of the nozzle. As expected, in positions close to the face-plate, large variation of the heat flux value along the perimeter occur due to the higher temperature stratification. On the other hand for axial positions closer to the exit (after 200 mm), the simulation demonstrates a flat heat flux profile, in agreement with the temperature field (Fig. 9), which becomes homogeneous.

An interesting effect is that the heat flux has a local minimum at the position directly above the injector ( $0^\circ$ ) and its maximum at approximately  $15^\circ$ . This effect starts after about 50 mm downstream of the injector and continues for the rest of

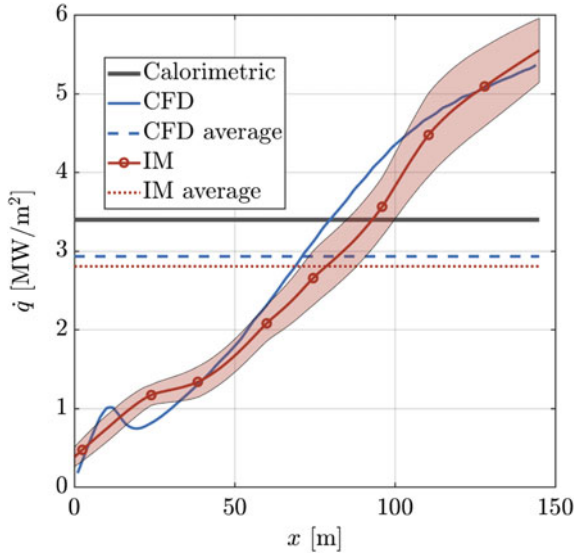


**Fig. 10** Axial and average heat flux profile for the CFD simulation and the inverse method. The calorimetric method is also shown for reference

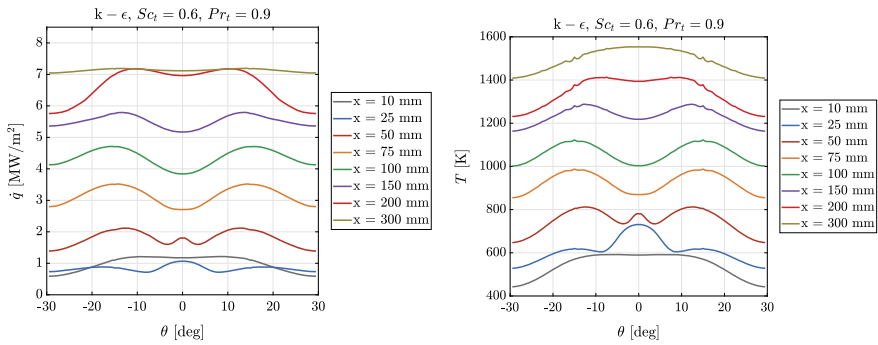


**Fig. 11** Heat flux (left) and temperature (right) variation along the chamber angle for different axial positions

the chamber and is similar to the experimental results reported in Sect. 4 and shown again in Fig. 12.

Some discrepancies are however noticed in the qualitative form of the profiles. It is evident that the low resolution of the inverse method caused by the positioning of the thermocouples does not allow for a detailed profile as in the case of the CFD. Specifically, the presence of a complicated pattern for positions between two injector elements (0° and 60°) is visible. Since this large-scale structure is finer than the resolution allowed by the thermocouple installation, this cannot be detected experimentally.

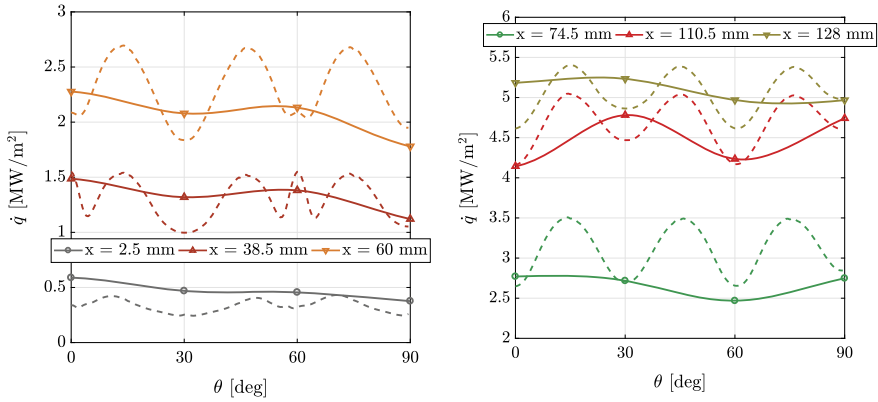


**Fig. 12** Heat flux profiles along the azimuthal direction for different axial positions for the inverse method (solid line) and the CFD simulation (dashed line)

Despite the inverse method profiles being coarser, they are still able to capture some of the effects found in the CFD. Starting with the first positions close to the face-plate (left sub-figure), both CFD and inverse method show a higher heat flux above the injectors ( $0^\circ, 60^\circ$ ) than between them ( $30^\circ, 90^\circ$ ). An additional local maximum at the  $\pm 10^\circ$  positions left and right of each injector is also a result of the CFD simulation. For the positions further downstream (right sub-figure), both methods show a shift in the maximum location. After 110 mm, the CFD heat flux values appear to shift, leading to global minima directly above the injector locations ( $0^\circ$  and  $60^\circ$ ). The main culprit for this change of the pattern is the increasing interaction of neighboring jets, which leads to hot gas being pushed towards the wall between the elements. It is hence quite assuring that the pattern observed in the inverse results and which was described in detail in Sect. 4.1, is not an artifact of the thermocouple measurements but rather a physical phenomenon supported by the CFD result.

In order to better understand the origin of this phenomenon, the temperature at the wall-next cell of the CFD calculation is plotted as seen in Fig. 11. At the wall position, the mixture fraction variance and the scalar dissipation tend to zero and hence the temperature becomes a function of the mixture fraction solely (and the enthalpy, which however does not alter the chemical composition in the adiabatic flamelet formulation).

As expected, the temperature has a maximum directly at the positions where the heat flux is also maximal and a minimum at  $0^\circ$ . This is a result of the mixture fraction profiles at the wall: after the stoichiometric mixture fraction  $Z_{st} = 0.2$ , the temperature decreases with increasing mixture fraction and hence, the local maximum of the heat flux corresponds to a lower value of  $Z$ , i.e. a leaner composition and vice versa. This is validated in Figs. 13 and 14. For positions closer to the injector, a recirculation zone is created which leads to a maximum in temperature and heat flux right above the injector. Further downstream pockets of fuel-rich mixture are created directly at  $0^\circ$  which lead to a decrease in temperature and heat flux. The shift in mixture fraction



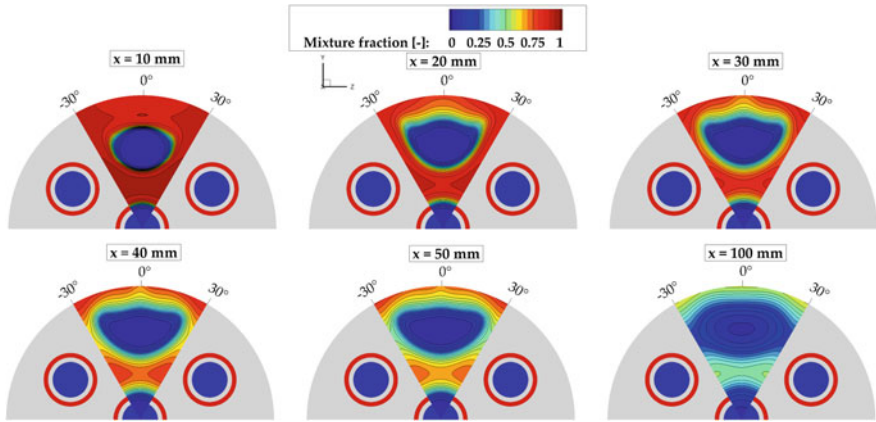


Fig. 13 Contour plot of mixture fraction at different planes in the thrust chamber

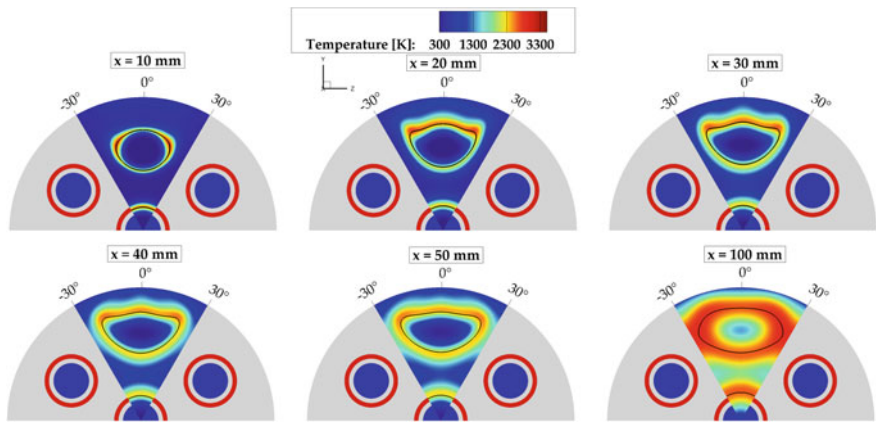
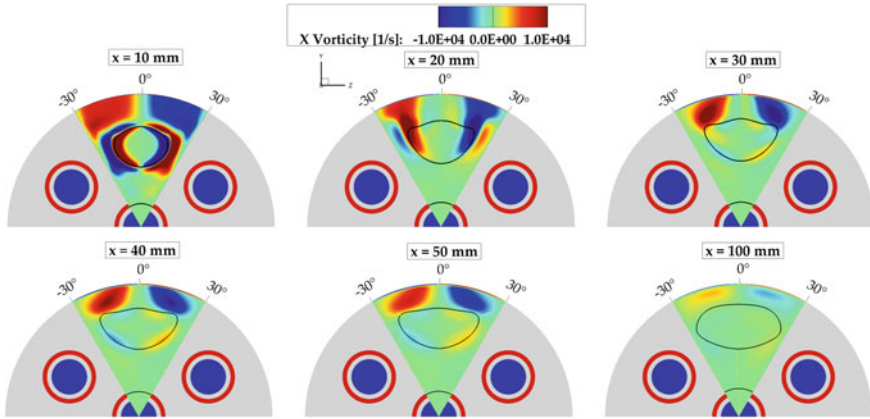


Fig. 14 Contour plot of temperature at different planes in the thrust chamber

values above the injector is also visible in Fig. 13. Up until  $x = 50$  mm, the mixture fraction at  $0^\circ$  is smaller than between the injectors and downstream of that point, a shift occurs leading to “colder”, high- $Z$  gas pockets being concentrated at  $0^\circ$ .

The presence of a strong vortex system feeding the hot, oxidizer-rich fuel towards the wall at the  $\pm 10\text{--}15^\circ$  position is visible when examining the vorticity field in the chamber. Specifically, the vorticity component along the axial direction  $\Omega_x = \frac{\partial u_z}{\partial y} - \frac{\partial u_y}{\partial z}$  is shown at selected planes in Fig. 15. Starting close to the faceplate (at  $x = 20$  mm) two locations with strong vorticity components appear at  $\pm 10 - 15^\circ$ . This system of vortices appears to circulate hot gas from the shear layer of the coaxial injector directly onto the wall and serves as the main driving force for the increased heat transfer coefficient at this angular position. Moreover this explains the shape of the temperature field in Fig. 14. In the first 10 mm from the faceplate, the interaction



**Fig. 15** Contour plot of vorticity at different planes in the thrust chamber

between the individual flames is weak and the expansion of the flame occurs nearly cylindrical, homogeneously in all radial directions. As soon as the jet-jet interaction is strengthened, the temperature field becomes distorted and the expansion occurs preferably upwards towards the wall. The vortex system which is responsible for this distortion is a consequence of the radial expansion of the individual jets and enhances the local heat loads between the injectors.

At positions further downstream, the presence of the vortex system is still visible but it appears to weaken after approximately 100 mm. At those positions the individual jets are no longer dominant and a homogeneous flow is achieved, which explains the absence of a strong recirculation zone. Due to the lack of a driving force for a circulation of hot gas towards the wall, at positions downstream of 100 mm the temperature and heat flux distribution appears to smoothen, leading to a flatter profile.

## 6 Conclusions

The evaluation of heat flux profiles in sub-scale engines is crucial for the understanding of the underlying physical and chemical processes defining the injector performance, the injector/injector and injector/wall interaction, mixing and energy release in the chamber. The inverse heat transfer method presented in this work is intended for the analysis of temperature and heat flux distributions in actively cooled rocket thrust chambers.

Similar to previous methods used for the estimation of heat fluxes in capacitive hardware, the inverse method relies on an iterative optimization method with the objective of minimizing the temperature difference between the measured and the calculated values. The update of the heat flux parameters at each iteration is carried

out using a pre-calculated Jacobi matrix via the Newton–Raphson method. This results to a very efficient optimization algorithm requiring minimal computational resources. The use of thermocouple measurements at different circumferential and axial positions allows for the resolution of axially and azimuthally varying heat loads.

The method can complement calorimetric methods for the evaluation of experimental tests, as it can resolve axially varying loads with much higher spatial accuracy. Studies are planned in order to improve the Nusselt correlations by adjusting them to the specific flow conditions examined.

The attractiveness of the new method is its ability to also resolve the azimuthal variation of the heat flux. Using the coarsest possible thermocouple installation in circumferential direction, it was shown that injector footprints can be obtained. This gives information about the interaction of the injector elements without the need for the repetition of the experiments with rotation of the hardware as was proposed by previous methods.

When applied for the evaluation of a GCH<sub>4</sub>/GOX multi-injector rocket combustor operated at 20 bar, insights into the physical phenomena in the chamber were obtained. An interesting effect in the circumferential heat flux profile is an observed shift in the location of the local maxima, occurring at around 70 mm distance from the injection plane. This also appeared to be in agreement with CFD simulations of the same load point and can be explained by the secondary flow structures created by the flame/flame interaction.

## References

1. Artioukhine, E.: Heat transfer and inverse analysis. RTO-EN-AVT-117 (2005)
2. Asakawa, H., Nanri, H., Aoki, K., Kubota, I., Mori, H., Ishikawa, Y., Kimoto, K., Ishihara, S., Ishizaki, S.: The status of the research and development of LNG rocket engines in japan. In: *Chemical Rocket Propulsion*, pp. 463–487. Springer, Berlin (2017)
3. Bird, R.B., Stewart, W.E., Lightfoot, E.N.: *Transport Phenomena*. Wiley, New York (1960)
4. Coy, E.B.: Measurement of transient heat flux and surface temperature using embedded temperature sensors. *J. Thermophys. Heat Transf.* **24**(1), 77–84 (2010)
5. Cuoco, F., Yang, B., Oswald, M.: Experimental investigation of LOX/H<sub>2</sub> and LOX/CH<sub>4</sub> sprays and flames. In: *24th International Symposium on Space Technology and Science* (2004)
6. Fletcher, R.: *Practical methods of optimization*. Wiley, New York (2013)
7. *Fluent: 18.0 ANSYS Fluent Theory Guide 18.0*. Ansys Inc (2017)
8. Frey, M., Aichner, T., Görden, J., Ivancic, B., Kniesner, B., Knab, O.: Modeling of rocket combustion devices. In: *10th AIAA/ASME Joint Thermophysics and Heat Transfer Conference*, p. 4329. AIAA Paper 2009-5477 (2010). <https://doi.org/10.2514/6.2009-5477>
9. Grisch, F., Bertseva, E., Habiballah, M., Jourdanneau, E., Chaussard, F., Saint-Loup, R., Gabard, T., Berger, H.: CARS spectroscopy of CH<sub>4</sub> for implication of temperature measurements in supercritical LOX/CH<sub>4</sub> combustion. *Aerospace Sci. Technol.* **11**(1), 48–54 (2007)
10. Haidn, O.J., Adams, N., Radespiel, R., Schröder, W., Stemmer, C., Sattelmayer, T., Weigand, B.: Fundamental technologies for the development of future space transport system components under high thermal and mechanical loads. In: *54th AIAA/SAE/ASEE Joint Propulsion Conference*, p. 4466 (2018)
11. Hirschfelder, J.O., Curtiss, C.F., Bird, R.B., Mayer, M.G.: *Molecular Theory of Gases and Liquids*. Wiley, New York (1954)

12. Kato, T., Terakado, D., Nanri, H., Morito, T., Masuda, I., Asakawa, H., Sakaguchi, H., Ishikawa, Y., Inoue, T., Ishihara, S., et al.: Subscale firing test for regenerative cooling LOX/methane rocket engine. In: 7th European Conference for Aeronautics and Space Sciences (EUCASS) (2017)
13. Kirchberger, C., Wagner, R., Kau, H.P., Soller, S., Martin, P., Bouchez, M., Bonzom, C.: Prediction and analysis of heat transfer in small rocket chambers. In: 46th AIAA Aerospace Sciences meeting and Exhibit, AIAA-2008-1260, Reno (NV), USA, pp. 07–11 (2008). <https://doi.org/10.2514/6.2008-1260>
14. Kirchberger, C.U.: Investigation on heat transfer in small hydrocarbon rocket combustion chambers. Ph.D. thesis, Technische Universität München (2014)
15. Knab, O., Frey, M., Görgen, J., Quring, K., Wiedmann, D., Mäding, C.: Progress in combustion and heat transfer modelling in rocket thrust chamber applied engineering. In: 45th AIAA/ASME/SAE/ASEE Joint Propulsion Conference & Exhibit, p. 5477 (2009)
16. Launder, B.E., Spalding, D.B.: *Mathematical Models of Turbulence*. Academic, London (1972)
17. Lemmon, E., McLinden, M., Friend, D., Linstrom, P., Mallard, W.: NIST chemistry WebBook, Nist standard reference database number 69. National Institute of Standards and Technology, Gaithersburg (2011)
18. Lux, J., Suslov, D., Bechle, M., Oschwald, M., Haidn, O.J.: Investigation of sub-and super-critical LOX/methane injection using optical diagnostics. In: 42nd AIAA/ASME/SAE/ASEE Joint Propulsion Conference & Exhibit (AIAA 2006-5077)
19. Perakis, N., Haidn, O.J.: Inverse heat transfer method applied to capacitively cooled rocket thrust chambers. *Int. J. Heat Mass Transf.* **131**, 150–166 (2019)
20. Perakis, N., Rahn, D., Haidn, O.J., Eiringhaus, D.: Heat transfer and combustion simulation of seven-element o<sub>2</sub>/ch<sub>4</sub> rocket combustor. *J. Propuls. Power* **35**(6), 1080–1097 (2019)
21. Perakis, N., Strauß, J., Haidn, O.J.: Heat flux evaluation in a multi-element ch<sub>4</sub>/o<sub>2</sub> rocket combustor using an inverse heat transfer method. *Int. J. Heat Mass Transf.* **142**, 118, 425 (2019)
22. Shim, M., Noh, K., Yoon, W.: Flame structure of methane/oxygen shear coaxial jet with velocity ratio using high-speed imaging and OH\*, CH\* chemiluminescence. *Acta Astronautica* **147**, 127–132 (2018)
23. Silvestri, S., Celano, M.P., Schlieben, G., Haidn, O.J.: Characterization of a multi-injector gox-gch<sub>4</sub> combustion chamber. In: 52nd AIAA/SAE/ASEE Joint Propulsion Conference. American Institute of Aeronautics and Astronautics, AIAA Paper 2016-4992 (2016). <https://doi.org/10.2514/6.2016-4992>
24. Slavinskaya, N., Abbasi, M., Starcke, J.H., Mirzayeva, A., Haidn, O.J.: Skeletal mechanism of the methane oxidation for space propulsion applications. In: 52nd AIAA/SAE/ASEE Joint Propulsion Conference, p. 4781. American Institute of Aeronautics and Astronautics, AIAA Paper 2016-4781 (2016). <https://doi.org/10.2514/6.2016-4781>
25. Suslov, D., Arnold, R., Haidn, O.: Investigation of film cooling efficiency in a high pressure subscale lox/h<sub>2</sub> combustion chamber. In: 47th AIAA/ASME/SAE/ASEE Joint Propulsion Conference & Exhibit, p. 5778. AIAA 2011-5778 (2011). <https://doi.org/10.2514/6.2011-5778>
26. Suslov, D., Betti, B., Aichner, T., Soller, S., Nasuti, F., Haidn, O.: Experimental investigation and CFD-simulation of the film cooling in an O<sub>2</sub>/CH<sub>4</sub> subscale combustion chamber. In: Space Propulsion Conference (2012)
27. Vaidyanathan, A., Gustavsson, J., Segal, C.: One-and three-dimensional wall heat flux calculations in a O<sub>2</sub>/H<sub>2</sub> system. *J. Propuls. Power* **26**(1), 186–189 (2010)
28. Wilke, C.: A viscosity equation for gas mixtures. *J. Chem. Phys.* **18**(4), 517–519 (1950). <https://doi.org/10.1063/1.1747673>
29. Wolfshtein, M.: The velocity and temperature distribution in one-dimensional flow with turbulence augmentation and pressure gradient. *Int. J. Heat Mass Transf.* **12**(3), 301–318 (1969). [https://doi.org/10.1016/0017-9310\(69\)90012-X](https://doi.org/10.1016/0017-9310(69)90012-X)

**Open Access** This chapter is licensed under the terms of the Creative Commons Attribution 4.0 International License (<http://creativecommons.org/licenses/by/4.0/>), which permits use, sharing, adaptation, distribution and reproduction in any medium or format, as long as you give appropriate credit to the original author(s) and the source, provide a link to the Creative Commons license and indicate if changes were made.

The images or other third party material in this chapter are included in the chapter's Creative Commons license, unless indicated otherwise in a credit line to the material. If material is not included in the chapter's Creative Commons license and your intended use is not permitted by statutory regulation or exceeds the permitted use, you will need to obtain permission directly from the copyright holder.

